Earth and Planetary Science Letters 452 (2016) 227–237

Contents lists available at ScienceDirect

Earth and Planetary Science Letters

www.elsevier.com/locate/epsl

Titanium-hydroxyl defect-controlled rheology of the Earth's upper mantle

Ulrich H. Faul [a,b,*], Christopher J. Cline II [b], Emmanuel C. David [b,1], Andrew J. Berry [b], Ian Jackson [b]

[a] *Earth Atmospheric and Planetary Sciences, Massachusetts Institute of Technology, Cambridge, MA, USA*
[b] *Research School of Earth Sciences, Australian National University, Canberra, Australia*

ARTICLE INFO

Article history:
Received 11 February 2016
Received in revised form 7 June 2016
Accepted 10 July 2016
Available online 18 August 2016
Editor: B. Buffett

Keywords:
upper mantle
deformation
olivine
water
defects
FTIR spectroscopy

ABSTRACT

Experiments were conducted with hydrous olivine to investigate the defect responsible for the influence of water (hydrogen structurally incorporated as hydroxyl) on the olivine rheology. Solution–gelation derived Fo_{90} olivine doped with nominally 0.04–0.1 wt.% TiO_2 was first hot-pressed and then deformed in platinum capsules at 300 MPa confining pressure and temperatures from 1200–1350 °C. The water content was not buffered so that deformation occurred at water-undersaturated conditions. Due to the enhanced grain growth under hydrous conditions, the samples were at least a factor of three more coarse-grained than their dry counterparts and deformed in powerlaw creep at differential stresses as low as a few tens of MPa. Since all experiments were conducted at the same confining pressure, the essentially linear relationship between strain rate and water content was for the first time determined independently of an activation volume. Infrared spectra are dominated by absorption bands at 3572 and 3525 cm^{-1}. These bands also predominate in infrared spectra of natural olivine, and can only be reproduced experimentally in the presence of titanium. In contrast to the previous interpretation of the hydrous rheology in terms of intrinsic point defects, the experiments show that extrinsic defects (impurities) in natural olivine play the dominant role for water weakening at the water contents expected for most of the upper mantle.

1. Introduction

It is well established that olivine deformed in the presence of water is weaker than when deformed under dry conditions (Avé Lallemant and Carter, 1970; Chopra and Paterson, 1984; Mackwell et al., 1985; Karato et al., 1986; Mei and Kohlstedt, 2000a, 2000b). These studies confirmed a relationship between the presence of water and strength, but because experiments were always carried out under water-saturated conditions the relationship between water fugacity and strength were not determined independently of confining pressures (Hirth and Kohlstedt, 2003; Karato and Jung, 2003).

Less clear is the point defect mechanism for weakening due to water. Fits to experiments at a range of pressures yielded a relationship between strain rate and water fugacity (fH_2O) with an exponent r as $\dot{\epsilon} \propto fH_2O^r$. Models of point defects were then examined to obtain the same exponent through a combination of the dominant defect for charge neutrality and diffusive accommodation of strain (Karato, 1989a; Mei and Kohlstedt, 2000a, 2000b). The hydrous defects thus inferred can not be readily reconciled with infrared absorption spectra from experiments aimed at correlating absorption bands with particular defects (Matveev et al., 2001; Lemaire et al., 2004; Berry et al., 2005). The defect models for deformation considered only intrinsic defects (vacancy and interstitial O, Mg, Fe^{2+}, Si, Fe^{3+} on octahedral and tetrahedral sites, and electrons, Kohlstedt and Mackwell (1998)). By contrast, natural olivine contains a range of impurities with abundances in the ppm range (extrinsic defects, de Hoog et al. (2010), Foley et al. (2013)). Previous experiments showed that titanium is required to experimentally reproduce the infrared spectra typical of natural samples (Berry et al., 2005). Ab inito modelling indicated that the associated hydrous defect is the most stable defect, potentially affecting the strength of olivine (Walker et al., 2007).

The experiments described in the following were carried out with Ti-doped olivine to investigate the role of this impurity on the rheology under hydrous conditions. The use of Pt capsules and $Ni_{70}Fe_{30}$ foils permitted water retention at a range of water contents at fixed confining pressure. The experiments were con-

---

[*] Corresponding author.
E-mail address: hufaul@mit.edu (U.H. Faul).

[1] Now at: Department of Earth Sciences, University College London, London, UK.

http://dx.doi.org/10.1016/j.epsl.2016.07.016
0012-821X/

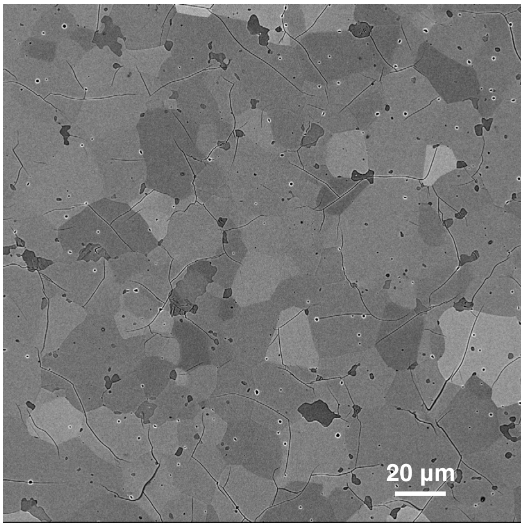

Fig. 1. Representative scanning electron microscope backscattered-electron image of the microstructure after hotpressing (prior to deformation). The grayscale variation of olivine crystals is due to orientation contrast. Darker patches predominantly on olivine grain boundaries and corners are orthopyroxene grains. Small orthopyroxene grains are also incorporated into olivine during growth from an estimated grain size of 1 μm prior to hotpressing. Cracks originate during cooling due to the thermal expansion anisotropy of olivine. Small pores inside olivine grains stand out due to their bright rim.

ducted at water-undersaturated conditions corresponding to those for most of the upper mantle. Infrared spectra were used to determine the water content and identify the hydrous defect associated with the observed water weakening.

2. Sample materials and experimental setup

The starting materials for the experiments were prepared by a solution–gelation process, resulting in fine-grained, chemically pure and homogeneous precursors (Faul and Jackson, 2007). For this study, Ti was added as tetra-ethoxy orthotitanate (TEOT, Berry et al., 2007b). The amount of Si in the gel was in excess of stoichiometric olivine (Fo_{90}) composition to ensure Si saturation (Fig. 1). After drying of the solution, the raw powders were reacted at 875 °C and repeatedly fired at 1200 °C and an fO_2 near the CCO buffer for more than 12 h. The powders were cold pressed into pellets that were again fired at an fO_2 near the CCO buffer and kept in a drying oven until wrapping in ~70 μm thick $Ni_{70}Fe_{30}$ foil (with nominally either 0.04 or 0.1 wt.% TiO_2 added) or encapsulation in laser-welded Pt capsules (0.04 wt.% TiO_2 added, with a foil thickness of 180 μm and 250 μm for hotpressing and deformation experiments, respectively). Table 1 provides a summary of experimental conditions and compositions. Each wrapped/encapsulated sample was inserted in a mild steel jacket and hot-pressed for 24 h at the same temperature as the subsequent deformation experiment. The temperature uncertainty is estimated as ±10 °C from regular furnace calibrations. All experiments were carried out at a confining pressure of 300 MPa.

After hot-pressing, the jacket was dissolved in acid, the Pt capsule peeled off and a ~1 mm thick slice was sectioned about 1.5 mm from the top end of the sample for microstructural examination and Fourier transform infrared (FTIR) spectroscopy. Each fully dense sample was precision ground to a cylinder with a diameter of 11.5 mm and a lengths near 25 mm before being refired at CCO and 1200 °C for 12 h prior to re-encapsulation for deformation. The deformation experiments were carried out in a gas medium (Paterson) apparatus under triaxial compression in a pre-programmed sequence of constant load segments, with load increasing after each segment. The load (force) was measured internally, displacements externally. Further details on the apparatus calibration and deformation procedures are given in Faul and Jackson (2007). After deformation a horizontal slice about 1 mm thick and 1.5 mm from the top or bottom end of each sample was prepared for microstructural and analytical examination.

The total strain for samples 6652 and 6656 with 0.1 wt.% Ti and deformed in $Ni_{70}Fe_{30}$ foils after the first 'staircase' of constant load was relatively small. Therefore, the load was reduced to zero and a second pass was programmed. This second pass provides a measure of the reproducibility of the strain rates. Similarly, 6795 with modest total strain was deformed again as 6803 after precision grinding to 10 mm diameter and 20 mm length, firing at 1200 °C at CCO conditions and re-encapsulation in Pt. Samples that were deformed to relatively high strains (6767 and 6803) began to flow around the pistons at both ends. In some instances canting was observed as a consequence of deformation.

3. Analytical methods

The samples were examined optically, by scanning electron microscopy (SEM), electron back-scatter diffraction (EBSD), electron probe micro-analysis (EPMA), laser ablation inductively coupled mass spectrometry (LA-ICPMS) and FTIR spectroscopy. Imaging and EBSD mapping were performed using a Zeiss Ultra Plus field emission scanning electron microscope at the Center for Advanced Microscopy at ANU. The EBSD maps were collected with an Oxford Instruments camera and HKL software from carbon coated samples at 20 kV acceleration voltage and 5 nA beam current. The maps consist of 400×400 or 450×450 points with indexing rates usually near 80%. The maps were processed with MTEX software. The grain sizes were determined from the EBSD maps as the equivalent diameter of a circle with the same area of each grain in the map. A sectioning correction factor of $4/\pi$ was applied to obtain the mean diameters in Table 1.

Microprobe analyses were performed using the CAMECA SX100 microprobe at RSES, ANU on selected samples to determine the Mg# (the molar ratio $100 \times Mg^{2+}/(Mg^{2+} + Fe^{2+})$). LA-ICPMS was performed at RSES ANU with an Excimer laser and a single collector mass spectrometer (Agilent 7700) with a spot size of 70 μm to determine the Ti contents in olivine given in Table 1. We also analysed a NIST 610 glass as a standard.

FTIR spectroscopy and the determination of the water content are detailed in Appendix A. Briefly, we measured the absorbance on 400 micron thick sections to enable measurements even at low water contents. Molecular water and hydroxyl contents were determined separately from the spectra. For the hydroxyl content we used the site-specific absorption coefficient from Kovacs et al. (2010), which is similar to the coefficient of Bell et al. (2003). The water content given in Table 1 is averaged from 25–30 measurements on radial traverses.

4. Results

4.1. Composition, microstructure and water content

After hotpressing, the samples are characterised by a near ideal 'foam' microstructure (Fig. 2a) with equant crystalline grains and a relatively narrow grain size distribution (Fig. 3, left). Orthopyroxene, derived from the excess silica in the gel as well as from grinding of the powders in agate mortars, is relatively homogeneously distributed as small grains located frequently at olivine grain corners (Fig. 1). Grain growth rates for water-bearing samples are significantly faster than for dry samples (Table 1, Karato, 1989b), with growth rates modulated by the orthopyroxene grains. Grains with non-uniform orientation (coloured in Fig. 2a) indicate coalescence of neighbours.

Table 1
Summary of experiments.

Sample	Wrapper/capsule	T (°C)	d[a] µm	Water			Titanium		Stress (MPa)	Strain (%)[f]
				Structural		Molecular	ppm Ti/Si[d]	wt. ppm[e]		
				ppm H/Si[b]	ppm H_2O[c]	ppm H/Si[b]				
6652	$Ni_{70}Fe_{30}$	1278	23.8	100(38)	6	0	1940	635	18–220	9
6656	$Ni_{70}Fe_{30}$	1200	29.8	10(6)	0.6	0	1940	635	114–320	16
6713	$Ni_{70}Fe_{30}$	1300	6.7	0	0	0	660	216	20–75	2.5
6714	$Ni_{70}Fe_{30}$	1200	6.5	0	0	0	660	216	75–100	2.1
6774	Pt	1200	20.0	490(280)	30	86(62)	798	261	37–241	13
6767	Pt	1200	15.9	724(140)	45	179(76)	798	261	65–213	37
6795	Pt	1250	40.0	542(370)	33	181(180)	866	283	30–232	9
6754	Pt	1300	70.2	821(280)	50	119(110)	698	228	23–72	21
6803	Pt	1350	22.4	639(110)	39	564(140)	866	283	5–74	27

For stress, strain rate and strain data for each experiment see supplementary materials.

[a] Grain size determined from EBSD maps (sectioning corrected).

[b] Equivalent to the atomic ratio H/10^6Si. Average values from the radial transects of each sample. Values in parenthesis represent one standard deviation of the transects (see Appendix A).

[c] ppm H_2O by weight.

[d] Equivalent to the atomic ratio Ti/10^6Si.

[e] ppm Ti by weight.

[f] Total strain at the end of the experiment.

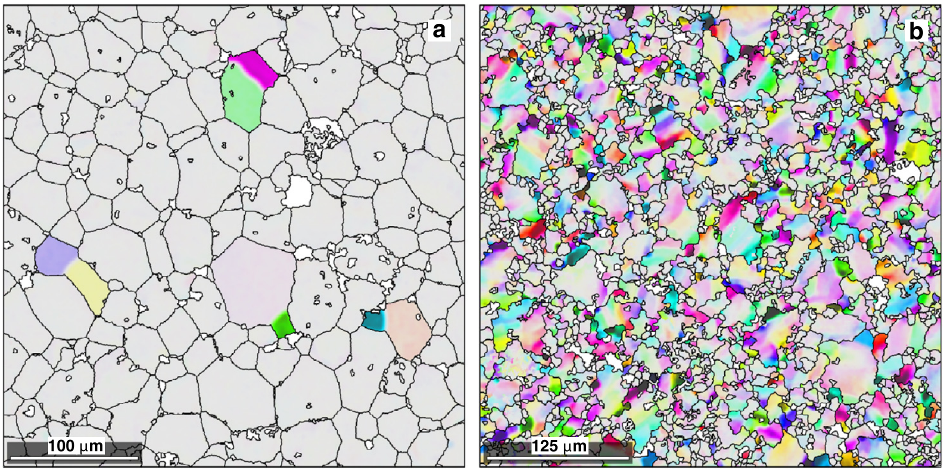

Fig. 2. EBSD maps of a hotpressed (a) and a deformed sample (b). Black lines show grain boundaries defined by misorientations of neighbouring pixels >10°. The colours represent grain internal misorientations relative to the mean orientation of each crystalline grain. White patches are not indexed areas and orthopyroxene grains. The hotpressed sample 6760 (a) has near ideal 'foam microstructure' with relatively equant grains and no grain internal deformation (gray). After deformation of this sample (b) the microstructure is characterised by extensive recrystallisation with mobile grain boundaries and strong grain internal deformation. The sample was deformed to a total strain of 37% (6767). (For interpretation of the references to colour in this figure legend, the reader is referred to the web version of this article.)

Samples deformed to relatively low strains experienced some grain growth during deformation, with grain size distributions that are similar to those after hotpressing (compare 6793 and 6795). Deformation to strains approaching or exceeding 30% leads to extensive recrystallisation with significant grain internal strain, complex grain shapes and interpenetrating grains (Fig. 2b) and significantly broader grain size distributions (Fig. 3).

Microprobe analyses of selected samples showed a uniform composition of the olivine with an average Mg# of 89.7 ± 0.5. The Ti content varies somewhat between different batches of the gel due to the difficulty in precisely adding small quantities of TEOT (one sample per batch was analysed by laser-ablation ICPMS). With two H per Ti atom expected for the titanium clinohumite-type point defect, comparison of the H and Ti contents in ppm/Si (Table 1) shows that typically less than half of the Ti is associated with protonated defects in the deformed materials. Water contents of hotpressed samples are higher (up to 1430 ppm H/Si or 88 wt. ppm H_2O), but remain at or below saturation of the Ti sites. The lower water content of deformed samples confirms that they are water-undersaturated during deformation.

FTIR spectra of samples doped with nominally 0.04 wt.% TiO_2 (the actual concentrations are given in Table 1) and hotpressed and deformed in Pt, show two distinct absorption bands at 3572 and 3525 cm^{-1}, indicating the presence of structurally bound hydrogen (hydroxyl). In addition a broad absorption region centred on 3450 cm^{-1} is observed in essentially all samples (Fig. 4). This broad absorption region corresponds to molecular water, likely contained in small pores (Fig. 1). Samples with 0.04 wt.% TiO_2 hotpressed and deformed in $Ni_{70}Fe_{30}$ foils are completely dry (e.g. 6713), while samples with a higher Ti content (nominally 0.1 wt.% TiO_2) in $Ni_{70}Fe_{30}$ foils retain small amounts of water after deformation (e.g. 6652).

Fe-bearing samples in contact with Pt are oxidised by the loss of Fe to the capsule (e.g. Jaques and Green, 1980 and references therein). The Fe content in olivine decreases from Fo_{90} in the interior to about Fo_{98} adjacent to the Pt capsule over a radial distance of about 100 µm, with a corresponding increase of the fO_2 from iron–wüstite (IW) + 2 in the interior to IW + 5 at the capsule. The interior of the samples is therefore to some extent self buffering. The fO_2 of $Ni_{70}Fe_{30}$ foil-wrapped samples is slightly above IW. We infer that the relatively high fO_2 and correspondingly high fH_2O and low fH_2 (Mackwell and Kohlstedt, 1990) adjacent to Pt capsules is necessary to retain hydrogen over the 8–24 h duration of the experiments without buffer. Hydrogen retention was not

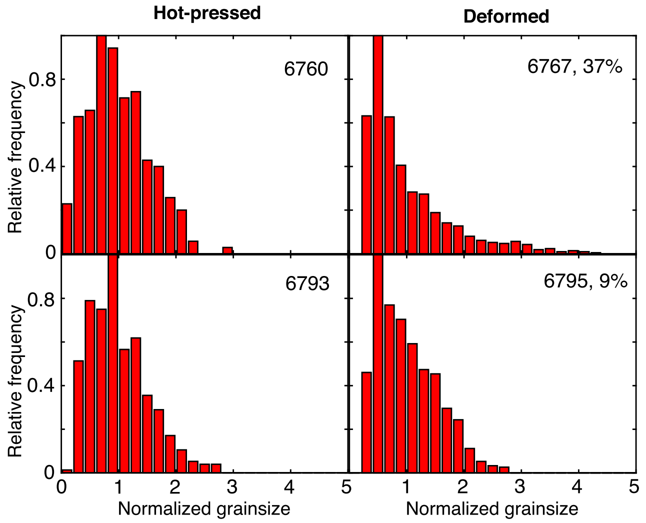

Fig. 3. Distributions of grain sizes normalized by the mean grain size of samples after hot-pressing and after deformation. The hotpressed samples have narrow grain size distributions, while distributions of the samples deformed to high strain (e.g. 6767) are much broader, indicating extensive recrystallisation. At 9% strain (6795) recrystallization is only incipient, and grain growth is still occurring.

observed in tests with Ni capsules with 0.04 wt.% TiO_2. Further details of the fO2 determination in sample interiors using dispersed Pt particles following the approach of Rubie et al. (1993) will be published separately.

4.2. Rheology

Rheological data are generally fitted to an empirical flow law of the form:

$$\dot{\epsilon} = A\,\sigma^n d^{-p} C_{\mathrm{OH}}^r \exp^{-(E+PV)/RT}, \qquad (1)$$

where $\dot{\epsilon}$ is the axial strain rate, σ the differential stress, d the grain size, A a constant, E the activation energy for creep, P pressure, T the (absolute) temperature, R the gas constant, n the stress exponent and p the grain size exponent (Mei and Kohlstedt, 2000b; Karato and Jung, 2003; Hirth and Kohlstedt, 2003). C_{OH} is the water content in units of ppm H/Si (i.e. H/10^6 Si) with exponent r. Values for the activation volume V were obtained from the literature (Hirth and Kohlstedt, 2003; Karato and Jung, 2003). Structurally bound hydrogen (hydroxyl) contents in our experiments after deformation range from 10 to 820 ppm H/Si (∼0.6 to 50 weight ppm water), with the lowest water contents observed for samples deformed in $Ni_{70}Fe_{30}$ foils (Table 1). With one exception, molecular water contents are significantly lower.

Plots of strain rate as a function of stress reveal two different deformational regimes (Fig. 5). A shallow slope at low stresses (most clearly seen in samples 6652 and 6803 in Fig. 5b) indicates diffusion creep with a linear stress and cubic grain size dependence in Equation (1). As a consequence of the coarse grain size of the starting aggregates, most of the data are consistent with a steeper slope and a stress exponent $n = 3.5$, a value that is characteristic of grain size-independent dislocation creep for olivine (Chopra and Paterson, 1984; Hirth and Kohlstedt, 2003). The most coarse-grained samples (mean grain sizes 40–70 μm) deform by dislocation creep at a stress below 50 MPa. This transition in the dominant deformation mechanism occurs at higher stresses for decreasing grain size. No grain size sensitivity is observed in this powerlaw creep regime for samples with grain sizes >15 μm.

For comparison with the experimental data, strain rates calculated with published flow laws (with parameters from Hirth and Kohlstedt (2003), those of Karato and Jung (2003) are similar) are shown by the solid lines in Fig. 5. For this calculation the hydroxyl contents in Table 1 were used (see Section 5.1). The pre-exponential constant for diffusion creep was increased to be consistent with the current results. All other parameters, including the activation energies and water content exponents, are the same as those obtained previously from water-saturated experiments at a range of confining pressures (Karato and Jung, 2003; Hirth and Kohlstedt, 2003).

Samples doped with ∼0.04 wt.% TiO_2 hotpressed and deformed in $Ni_{70}Fe_{30}$ foils do not contain detectable water (Fig. 4, 6713). Consistent with the absence of detectable water they remained fine-grained (<7 μm, Table 1). Their diffusion creep rheology is somewhat weaker than the rheology of undoped Fo_{90} solgel (Faul and Jackson, 2007), and can be modelled with the parameters in Table 2 with 5 ppm H/Si (Fig. 6). Ti by itself thus contributes only modestly to the enhanced strain rates of the experiments described here.

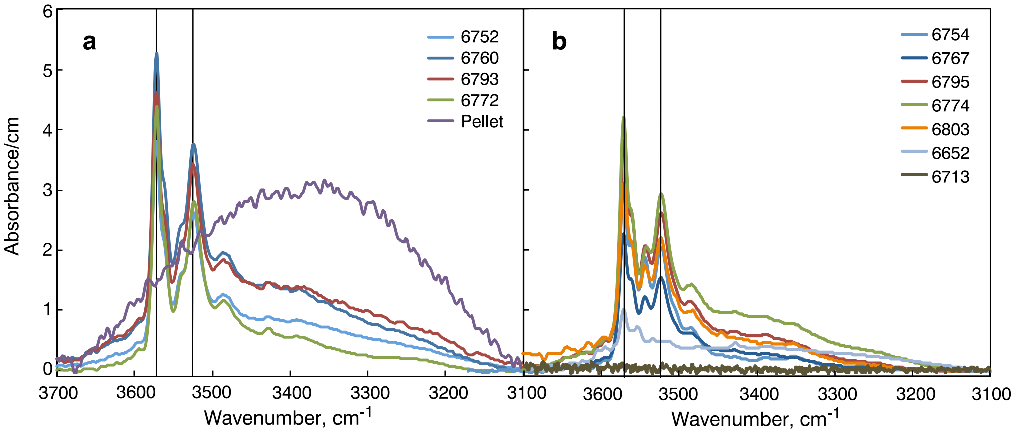

Fig. 4. Representative FTIR spectra of hotpressed (a) and deformed samples (b). The unpolarised absorption spectra were obtained from sections that are ∼400 μm thick. All samples show the absorption bands characteristic of the titanium–clinohumite like point defect (vertical lines at 3572 and 3525 cm^{-1}). The spectra were collected approximately 1.5 mm from the outer edge of the samples, except for $Ni_{70}Fe_{30}$ foil-wrapped 6652 (interior). In the post-deformation Pt encapsulated samples the outer regions typically have higher water contents compared to the interiors, while hotpressed samples have more uniform water contents. The water contents given in Table 1 are volumetric averages of concentric cylindrical volumes for which the water contents were determined from transects on the horizontal slices consisting of 25–30 spectra from centre to rim of each sample (see Appendix A). The spectrum labelled 'pellet' shows adsorbed water in cold pressed pellets after firing prior to encapsulation in Pt for hotpressing. The spectrum from 6713 shows an example from a $Ni_{70}Fe_{30}$ foil wrapped sample that is dry.

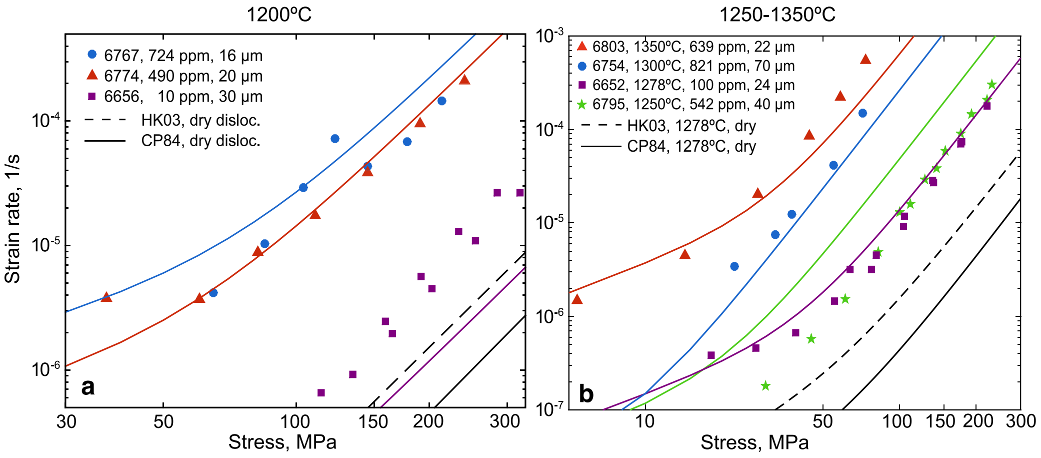

Fig. 5. Rheology of hydrous, Ti-doped olivine as a function of hydroxyl content. (a) 1200 °C data, and (b) data from 1250–1350 °C experiments. Symbols represent rheological data from this study (Supplementary Tables 1–5). Solid lines, with the same colour as the associated data points were calculated with the rheological parameters (Table 2, Hirth and Kohlstedt, 2003) for the water contents indicated in the legend for each sample in ppm H/Si. For reference, dry dislocation creep rheologies are indicated by solid black (Chopra and Paterson, 1984), and dashed lines (Hirth and Kohlstedt, 2003). The shallower slopes at low stress for some of the samples with grain sizes near 20 μm (e.g. 6652) indicate deformation by diffusion creep. The coarse-grained sample 6754 deforms by dislocation creep below 50 MPa. The noticeable deviation from the flow law (lines) of samples 6656 and 6795 likely reflects uncertainties in their water contents. (For interpretation of the references to colour in this figure legend, the reader is referred to the web version of this article.)

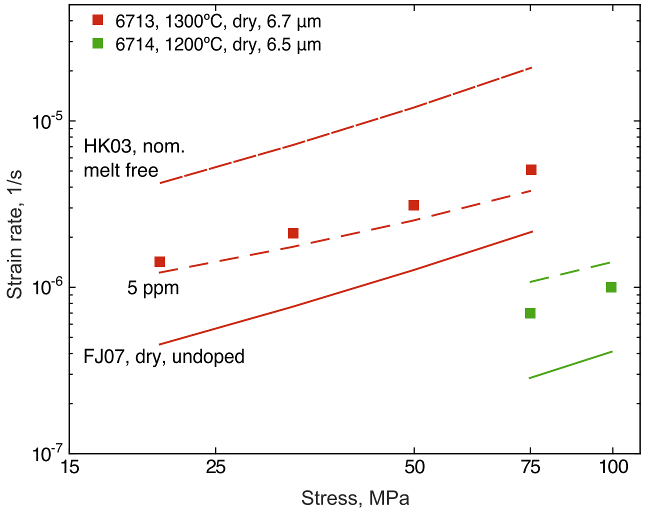

Fig. 6. Diffusion creep rheology of dry Ti-doped olivine. The samples are weaker than the undoped Fo_{90} rheology of Faul and Jackson (2007) (FJ07, solid lines), but stronger than the dry, nominally melt-free rheology of Hirth and Kohlstedt (1995), Hirth and Kohlstedt (2003) (HK03, long dashed shown for 1300° only). The strength of the dry, Ti-doped (0.04 wt.% TiO_2) samples is adequately described by the parameters in Table 2 with a water content of 5 ppm H/Si (dashed).

5. Discussion

5.1. Possible effect of molecular water

Experiments on silicon self-diffusion in olivine showed high diffusivities under dry conditions and only minor enhancements under water-undersaturated conditions (Fei et al., 2012, 2013), leading to the proposal that water has only a minor effect on the rheology of olivine. Previous deformation experiments on polycrystalline aggregates conducted with the aim of determining the effect of water on rheology were carried out with a buffer assembly to ensure that the samples remained water saturated (Mei and Kohlstedt, 2000a; Jung and Karato, 2001). FTIR spectra of these deformed polycrystalline samples are dominated by molecular water, which was presumed to reside in pores and at grain boundaries (Mei and Kohlstedt, 2000a). This free water was suggested to have contributed to the substantial reduction in creep strength compared to dry aggregates (Fei et al., 2013). Molecular water is absent at the water-undersaturated conditions of most of the Earth's upper mantle, raising the question of whether previous hydrous deformation experiments may have overestimated the effect of water on the rheology. The diffusion experiments showing little influence of water on diffusivity (Fei et al., 2013) were conducted with Ti-free synthetic forsterite (Fei et al., 2012), while earlier hydrous diffusion experiments finding a significant effect of water on diffusivity were conducted with Ti-bearing San Carlos olivine (Costa and Chakraborty, 2008).

Table 2
Flow law parameters (equation (1)).

	A (MPa^{-n} s^{-1} μm^p $C_{H_2O}^{-r}$)	n	p	r	E (kJ/mol)	V (10^{-6} m^3/mol)
Diffusion	4×10^5	1	3	1	335	4
Dislocation	90	3.5	0	1.2	480	11

Parameters (grain size in μm, stress in MPa and water contents in ppm H/Si) are from Hirth and Kohlstedt (2003), except the pre-exponential constant for diffusion creep, which has been adjusted to fit our data. The parameters of Karato and Jung (2003) are overall similar, but with a somewhat lower activation energy. Pre-exponential constant A in SI units: $A_{diff} = 4\times10^{-19}$ $Pa\,s^{-1}\,m^3\,C_{H_2O}^{-1}$, $A_{disloc} = 9\times10^{-20}$ $Pa^{-3.5}\,s^{-1}\,C_{H_2O}^{-1.2}$, for stress in Pa and grainsize in m. $r = 1$ and E 460 kJ/mol (A unchanged) for dislocation creep are also compatible with our data (Fig. 7).

Determining hydroxyl and molecular water contents separately enables examination of the measured strain rates as a function of these two components (Fig. 7). For this comparison the dislocation creep data were recalculated for a common temperature of 1200 °C and differential stress of 150 MPa with Equation (1) and the parameters in Table 2. Hirth and Kohlstedt (2003) infer that the transition from a 'wet' rheology to a 'dry' rheology occurs at a water content of 50 ppm H/Si (i.e. 50 H/10^6Si or ~3 weight ppm H_2O) based on their dry rheology. The somewhat lower strain rates observed by Chopra and Paterson (1984) for dry olivine imply a wet to dry transition at ~5 ppm H/Si. In diffusion creep this value for the wet to dry transition is supported by the rheology of dry, Ti-doped samples (Fig. 6). Hirth and Kohlstedt (2003) do not distinguish between molecular water and hydroxyl, so both rheologies are plotted at their respective inferred water content at the wet to dry transition.

Samples deformed in $Ni_{70}Fe_{30}$ foils contain no detectable molecular water, only small amounts of hydroxyl. If molecular wa-

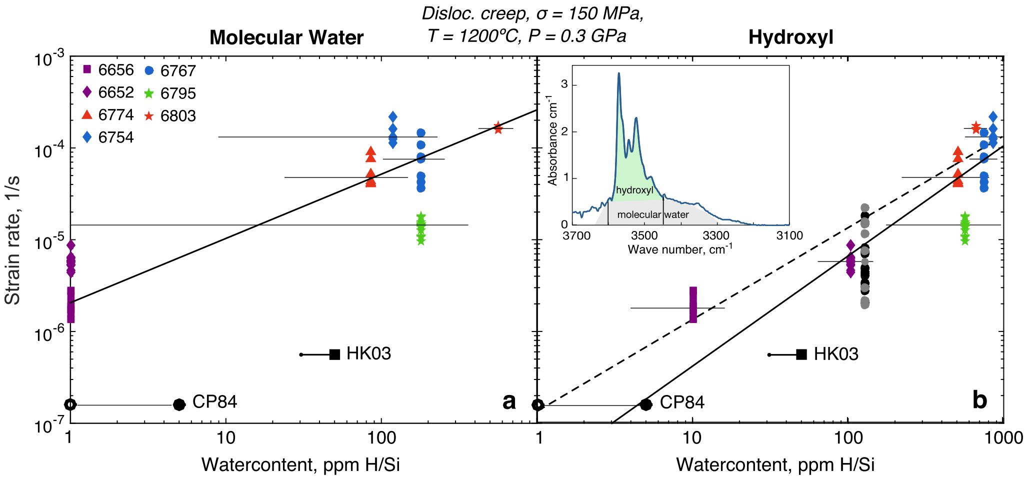

Fig. 7. Dislocation creep data for each sample recalculated for a common temperature of 1200 °C and a common stress of 150 MPa as a function of water content (Table 1). The scatter in strain rates after normalisation gives an indication of the uncertainty in the rheological data. Standard deviations of the 25–30 analyses per sample are shown as uncertainties in water contents (thin black lines). (a) Molecular water. A fit to the data of the present study requires $r \sim 0.7$ and constant $A \sim 7000$. However, a flow law with these values does not intersect the dry dislocation creep rheology (CP84, Chopra and Paterson, 1984, HK03, Hirth and Kohlstedt, 2003 (black symbols). (b) Structurally bound hydrogen (hydroxyl). The data is well described by the parameters given in Table 2 ($r = 1.2$) intersecting the dry rheology of Chopra and Paterson (1984) at 5 ppm H/Si. The dashed line indicates $r = 1$, $E = 460$ kJ/mol, intersecting the dry rheology at 1 ppm H/Si. Grey dots at 130 ppm H/Si are data from Mei and Kohlstedt (2000a), black dots from Tasaka et al. (2015) (see Section 5.4). Inset in (b) shows an FTIR spectrum from sample 6803 that contains contributions from hydroxyl (green, absorption bands at 3572 and 3525 cm^{-1}, black vertical lines indicate the limits of integration) and molecular water (gray). (For interpretation of the references to colour in this figure legend, the reader is referred to the web version of this article.)

ter controlled the rheology, these samples should have strain rates consistent with the published dry rheologies (Chopra and Paterson, 1984; Hirth and Kohlstedt, 2003) (Fig. 7a). A fit to the molecular water content of this study would have indeed a smaller water concentration exponent $r \sim 0.7$ relative to published fits (Hirth and Kohlstedt, 2003; Karato and Jung, 2003), but would not intersect the published dry rheologies. It is thus unlikely that the rheology of olivine is controlled by the molecular water content.

When plotted as a function of hydroxyl content, the experimental strain rates fall with some scatter on the strain rates calculated with Equation (1) based on published parameters for dislocation creep (Table 2, Fig. 7b). This flow law intersects the dry rheology of Chopra and Paterson (1984) at a hydroxyl content of ~5 ppm H/Si, indicating the transition to a dry rheology at this low water content. Alternatively if the wet to dry transition is assumed to occur at a hydroxyl content of 1 ppm H/Si the exponent r would have a value of one, together with a somewhat lower activation energy (460 kJ/mol).

The powerlaw rheology, lack of grain size sensitivity, and the recrystallisation observable in experiments with high strains (Fig. 2b) all point to a grain internal (dislocation) mechanism for deformation. This grain internal mechanism is not sensitive to the water content of grain boundaries. Fig. 7b shows that the hydroxyl content in the Ti-related absorption bands can explain the observed enhancement of the strain rates relative to dry conditions, rather than molecular water (Fei et al., 2013).

5.2. Structural site for hydrogen incorporation in olivine from IR spectra

Infrared spectra of natural olivine show more than 50 absorption bands between 3612 and 3160 cm^{-1} (e.g. Beran and Libowitzky, 2006 and references therein). These bands, due to absorption of infrared energy associated with the stretching of OH bonds, indicate that hydrogen is incorporated into the olivine crystal structure as a trace element at different defect sites with corresponding absorption bands. Experiments attempting to reproduce the natural spectra, and associate specific defects with individual absorption bands are complicated by the use of different starting materials, types of capsules and buffering conditions, and pressures at which they were conducted. In the following, different experiments and conditions are discussed to highlight their systematics.

Infrared spectra of samples of experiments with both natural and synthetic olivine exhibit differences attributed to silica activity (Matveev et al., 2001; Lemaire et al., 2004; Berry et al., 2005). At high silica activity (orthopyroxene buffered) bands are observed at wave numbers below 3400 cm^{-1}, in particular the high silica activity band at 3160 cm^{-1}. At low silica activity (magnesio-wüstite buffered) bands are observed between 3612 and 3430 cm^{-1}, with the most prominent bands at 3612, 3579 and 3567 cm^{-1} (Lemaire et al., 2004; Berry et al., 2005). The bands above wave numbers of 3400 cm^{-1} (group I bands of Bai and Kohlstedt (1993)) are therefore associated with tetrahedral (Si) site related defects, while the bands below 3400 cm^{-1} (group II bands of Bai and Kohlstedt (1993)) are associated with octahedral (M) site defects.

Doping synthetic forsterite with a range of trivalent cations results in absorption bands between 3400 and 3300 cm^{-1} (Berry et al., 2007a). The experiments show correlations between the location of the most intense absorption band and the ionic radius of the trivalent cation, and the concentration of a cation and the absorbance. Hydrogen associated with Fe^{3+} produces the most intense absorption bands at 3350 and 3331 cm^{-1} (Berry et al., 2007a), explaining the strong fO_2 dependence observed for the group II bands by Bai and Kohlstedt (1993), and the absence of these bands for olivine at low fO_2, even at high silica activity. Consistent with this interpretation, the experiments on Fo_{90} olivine in Pt capsules exhibit bands between 3400 and 3300 cm^{-1} (Matveev et al., 2001; Berry et al., 2005), while these bands are absent for Fo_{100} prepared under similar conditions (Lemaire et al., 2004; Berry et al., 2005).

The most ubiquitous, and frequently the only, bands observed in natural olivine from regions of the Earth's upper mantle that are far from water saturation and unaffected by hydrothermal alteration, are those at 3572 and 3525 cm^{-1} (Miller et al., 1987; Bell et al., 2003; Demouchy et al., 2006; Beran and Libowitzky, 2006; Peslier et al., 2010). These two bands are also the only ones observed in untreated San Carlos olivine (Mackwell et al., 1985; Bai and Kohlstedt, 1993; Berry et al., 2005). Spectra from experiments at 300 MPa confining pressure conducted with San Carlos olivine always include these two bands, among others (Mackwell et al., 1985; Mackwell and Kohlstedt, 1990; Bai and Kohlstedt, 1992, 1993; Kohlstedt and Mackwell, 1998; Mei and Kohlstedt, 2000a; Mei et al., 2002; Zhao et al., 2004; Tasaka et al., 2015).

Experiments with natural and synthetic olivine show that the bands at 3572 and 3525 cm^{-1} and their relative intensities can only be reproduced in either pure forsterite or Fo_{90} olivine if the samples contain Ti (Berry et al., 2005, 2007a; Padrón-Navarta et al., 2014). Because these bands occur at the same energies as two of the main bands of natural Ti-clinohumite, the defect is referred to as Ti-clinohumite-like point defect (see Berry et al., 2007b and references therein). San Carlos olivine contains 10–25 atom ppm Ti (equivalently 18–46 ppm Ti/Si, de Hoog et al. (2010), see below) and consequently exhibits the corresponding absorption bands under hydrous conditions. Experimental observations indicate that the Ti-related bands are present regardless of silica activity (Bai and Kohlstedt, 1993; Berry et al., 2005).

Absorption frequencies for hydrated defects calculated from first principles with quantum chemical methods are consistent with the experimental observations (e.g. Walker et al., 2007; Balan et al., 2011; Umemoto et al., 2011). Models of hydrated Si vacancies result in calculated absorption bands at frequencies >3450 cm^{-1}, while hydrated M-site vacancies result in bands at frequencies <3300 cm^{-1}. Walker et al. (2007) and Balan et al. (2011) confirm the Ti-defect as energetically the most favourable hydrous defect, with location of the bands and their polarisation, as well as site-specific absorbance consistent with observations.

In summary, the following hydrous defect types in olivine can be distinguished: tetrahedral- (Si), Ti-, octahedral- (Mg), and trivalent- (M^{3+}) related. This distinction was confirmed by the observation of different rates of change of band height and hence diffusivities for the different defects in diffusion experiments (Padrón-Navarta et al., 2014), as well as natural samples (Peslier et al., 2015).

In higher pressure experiments (>5 GPa) the most intense bands occur at 3612 and 3567 cm^{-1} (Kohlstedt et al., 1996; Mosenfelder et al., 2006), with a number of other peaks merging and producing broad absorbance in this region. The height of the most intense bands is several times greater than those in the 300 MPa experiments, indicating a higher solubility. The Ti-related bands, with absorbance limited by the amount of Ti in the San Carlos olivine used in the experiments, are subsumed into this broader absorption region.

A potential complication with the experimental assemblies of Kohlstedt et al. (1996) is that while they included orthopyroxene, the presence of pure forsterite in contact with Fo_{90} San Carlos olivine indicates that chemical equilibrium was not attained. As Si is slower to diffuse than Mg, and orthopyroxene was further away from the San Carlos olivine single crystal than the forsterite, it is possible that the Si-activity was not buffered. However, thermodynamic calculations suggest that at high fH_2O hydrated defects associated with Si will become increasingly important even with Si-buffering (Walker et al., 2007).

5.3. *Defect models for hydrous deformation*

The creep rate during deformation is limited by the diffusivity of the slowest ionic species diffusing along its fastest path. For diffusion by a vacancy mechanism the diffusivity of an ion depends on the concentration of this vacancy. The concentrations of point defects in turn are constrained by charge neutrality, which therefore needs to be considered in models of deformation. Intrinsic point defects in olivine include tetrahedral (Si), octahedral (M) and oxygen vacancies and interstitials (see also previous section).

Based on a range of experimental observations, under anhydrous conditions, the dominant charge neutrality condition for olivine is inferred to consist of Fe^{3+} on metal sites charge-balanced by metal site vacancies (Nakamura and Schmalzried, 1983; Karato, 1989a; Mei and Kohlstedt, 2000a; Kohlstedt, 2006), at least under oxidising conditions (Kohlstedt and Mackwell, 1998). In Kröger–Vink notation this is expressed as $[M_M^{\bullet}] = 2[V_M'']$, where square brackets indicate concentration, $M_M^{\bullet}$ a metal ion with a single excess positive charge on a metal site (i.e. Fe^{3+}), and V_M'' a metal site vacancy, implying two negative charges. Deformation of olivine is rate-limited by Si as the slowest diffusing ionic species (Jaoul et al., 1981; Hirth and Kohlstedt, 2003; Kohlstedt, 2006; Dohmen and Milke, 2010).

In the presence of water, protons (denoted by $p^{\bullet}$) affect defect concentrations and charge neutrality. The observation of enhanced strain rates implies that the concentration of Si vacancies is increased in order to increase Si diffusivity. The law of mass action can be used to show that the concentration of each point defect is proportional to the water fugacity to an exponent r: $[\ ] \propto (fH_2O)^r$ (Karato, 1989a; Mei and Kohlstedt, 2000a). Water fugacity can be converted to concentration by considering an activation enthalpy for the incorporation of hydroxyl (Kohlstedt et al., 1996; Keppler and Bolfan-Casanova, 2006).

With this approach, the dominant defects under hydrous conditions can then be obtained by comparing the experimentally determined exponent r in Equation (1), with that predicted by the combination of dominant defect for charge neutrality and involvement of tetrahedral site defects from the law of mass action (see e.g. Kohlstedt, 2006; Karato, 2008). The combination of doubly protonated Si vacancies, $(2H)_{Si}''$ with the charge neutrality condition $[p^{\bullet}] = [H_M']$ yields a water fugacity exponent of one, which is near the experimentally determined value of 1.2 (Kohlstedt, 2006). However, based on the observations presented in the previous section, this combination of defects also implies that the FTIR spectra should exhibit both tetrahedral (group I) and octahedral (group II) bands, which is not always the case (Bai and Kohlstedt, 1992, 1993; Kohlstedt and Mackwell, 1998; Girard et al., 2013), and not observed in this study. As an alternative model for $r \sim 1$ (Karato and Jung, 2003) consider positively charged jogs and silicon interstitials.

The above model originates with experiments conducted on iron bearing olivine at dry conditions using high purity oxides where fO_2 was varied (Nakamura and Schmalzried, 1983). Variation of fO_2 affects the Fe^{2+}/Fe^{3+} ratio, which lead to the conclusion that defects involving metal site vacancies are the dominant intrinsic defects. However, natural olivine contains a range of impurities such as Ti, Al, and Na, with oxidation states independent of fO_2 within the olivine stability field. Concentrations of these impurities range from a few wt. ppm to several hundred wt. ppm (de Hoog et al., 2010; Foley et al., 2013, see Section 6). By comparison, estimated concentrations of metal vacancies are of order of tens of ppm at anhydrous conditions (Nakamura and Schmalzried, 1983; Kohlstedt, 2006). The abundance of extrinsic defects is therefore comparable to that of the most abundant intrinsic defect (Dohmen and Chakraborty, 2007). The latter authors also pointed out the need to consider extrinsic defects in models of diffusion.

Titanium occurs as Ti^{4+} at mantle conditions, and X-ray absorption spectroscopy combined with ab initio calculations show that it occupies the Si site in dry olivine. On hydration Ti is octahedrally coordinated with two hydrogens on an adjacent silicon vacancy (Berry et al., 2007b; Walker et al., 2007). Hydration of the component Mg_2TiO_4 can be written as follows:

$$(Mg_2)_M(Ti)_{Si}O_4(ol) + H_2O$$
$$= (MgTi)_M(H_2)_{Si}O_4(\text{Ti-humite}) + MgO. \qquad (2)$$

In the presence of an enstatite buffer MgO will react further:

$$MgO + MgSiO_3 = Mg_2SiO_4. \quad (3)$$

Creation of a hydrous Ti-defect therefore increases the concentration of Si vacancies without affecting pre-existing (intrinsic) point defect concentrations. The above relations also show that hydration can occur regardless of oxide buffering. Equation (2) yields a linear dependence of concentration of the defect on fH_2O (Keppler and Bolfan-Casanova, 2006), consistent with a power-law exponent r near unity in Equation (1) (Table 2). The IR spectra (Fig. 4) show that at water-undersaturated and Si-buffered conditions only Ti defects are hydrated, but not metal or Si vacancies without an adjacent Ti, whose hydration evidently requires more energy (cf. Walker et al., 2007). While at higher pressures (and fH_2O at saturated conditions), other defect species dominate (Kohlstedt et al., 1996), at low pressure and at water-undersaturated conditions the Ti-clinohumite defect is the dominant defect and controls the effect of water on the olivine rheology. For the present experiments at fixed confining pressure and at water-undersaturated conditions, the directly measured water concentrations constrain the parameter r in Equation (1) (Fig. 7b).

5.4. *Rheology of hydrous San Carlos olivine*

As described above, FTIR spectra of San Carlos olivine always contain the Ti-related absorption bands. Trace element analyses of San Carlos olivine yield up to 46 ppm Ti/Si (de Hoog et al., 2010), implying about 90 ppm H/Si at saturation of the Ti defect. However, olivine from San Carlos can have a range of Mg# (Zhao et al., 2004), while the Ti concentrations of clinopyroxene are variable (Frey and Prinz, 1978), suggesting that the Ti content in olivine may also vary. Since the spectra showing structurally incorporated hydrogen in the experiments of Mei and Kohlstedt (2000a, 2000b) and Mei et al. (2002) were obtained from large single crystals embedded in a much more fine-grained matrix, the Ti content of the single crystals and matrix may also differ, particularly if matrix and single crystal have different Mg# (Tasaka et al., 2015). The actual Ti content of the experimental samples is not available.

Analysis of published infrared spectra (Bai and Kohlstedt, 1993; Mei and Kohlstedt, 2000a; Tasaka et al., 2015) with the procedure described in Appendix A yields an approximate water content of about 130 ppm H/Si associated with the Ti-defect (cf. inset in Fig. 7) for these experiments. This water content does not include hydroxyl in group II bands or molecular water, and is broadly consistent with the water content inferred from the Ti content above.

Rheological data from Mei and Kohlstedt (2000a, 2000b) and Tasaka et al. (2015) are shown in Fig. 8, along with strain rates calculated with the parameters from Table 2 and a water content of 130 ppm H/Si. As the figure shows, within the scatter of the data, the measured strain rates are consistent with those calculated based on the hydroxyl contents in the Ti-related defects in San Carlos olivine, explaining the consistency with our data.

5.5. *Experimental uncertainties*

Uncertainties arise primarily from possible temperature gradients along the length of the samples, as well as radial and longitudinal heterogeneities in water contents. Uncertainties in grain sizes will affect the diffusion creep data, but this is more of a problem for the dry samples with their smaller grain size. Temperature uncertainties are minimized (but not eliminated) by calibration experiments at regular intervals, typically before and after deformation experiments, so that possible changes in the temperature profile of the furnace can be accounted for. As described in Appendix A the water content for each sample given in Table 1 is averaged from volume weighted radial profiles. This may be the largest source of uncertainty and scatter seen in Figs. 5 and 7b.

6. Application to the upper mantle

The above discussion links water weakening of olivine to its Ti content. Before applying the experimentally determined rheology to the upper mantle, Ti contents in olivine from the upper mantle need to be considered. Ti contents in olivine vary from a few wt. ppm to ∼300 wt. ppm Ti (de Hoog et al., 2010; Peslier et al., 2010; Foley et al., 2013), with analyses being obtained predominantly from cratonic xenoliths. For comparison, the low Ti experiments contain ∼220 wt. ppm Ti (800 ppm Ti/Si, Table 1). Most xenoliths have a Mg# significantly above that expected for fertile upper mantle, indicating that the rocks were affected by melt extraction, which also decreases the Ti content. Subsequent metasomatism can increase the Ti content to well above pre-depletion levels (de Hoog et al., 2010; Foley et al., 2013). The data from de Hoog et al. (2010) suggests that olivine from garnet peridotite xenoliths on average contains more Ti relative to olivine from spinel peridotites.

The mid-ocean ridge basalt source upper mantle composition DMM includes olivine with a Mg#89.5 containing 102 wt. ppm Ti (Workman and Hart, 2005). For asthenospheric mantle, with two H per Ti, the maximum water content in olivine associated with the Ti defect (but not the total water storage capacity) is ∼600 ppm H/Si or about 40 wt. ppm H_2O.

Based on water contents of erupted mid-ocean ridge basalts, their mantle source was inferred to contain 50–200 wt. ppm H_2O (Michael, 1988; Tenner et al., 2012). Accounting for partitioning between the solid phases of the mantle, before the onset of melting the water content of olivine was estimated at 800–1000 ppm H/Si (Hirth and Kohlstedt, 1996), similar to the maximum water content in the present experiments. More recent determinations of the partition coefficient between olivine and pyroxene yielded estimates for olivine water contents as low as 360 ppm H/Si at 70 km depth (Tenner et al., 2012), which is below saturation of the Ti defect for the DMM composition. The Ti defect can therefore accommodate most or all of the water content predicted for olivine in the asthenosphere. The experiments presented here show that at water-undersaturated conditions this defect is the most stable hydrous defect and therefore the first to be hydrated.

Viscosities calculated with the parameters in Table 2 are shown in Fig. 9 contoured by water content at constant shear stress and grain size. As for seismic velocities (Faul and Jackson, 2005) the viscosity minimum occurs where the conductive geotherm joins the adiabat. Below the minimum, the rate of the viscosity increase with depth depends on the activation volume. For this combination of grain size (10 mm) and stress (0.3 MPa), dislocation creep dominates in the entire upper mantle for both wet and dry rheologies in the oceanic case.

Assuming water is the only variable affecting the rheology in addition to pressure and temperature, minimum viscosities $<10^{19}$ Pa s as inferred for example for the Western United States (Bills et al., 2007) or Iceland (Fleming et al., 2007) require water contents of >300 ppm H/Si at a stress of 0.3 MPa (Podolefsky et al., 2004). Water contents of up to 80 wt. ppm (∼1300 ppm H/Si) in olivine have been observed in high pressure cratonic xenoliths (Peslier et al., 2010), although not all water is associated with Ti. Potentially these high water contents have implications for the long term stability of cratons. However, high seismic velocities extending to significant depth and the absence of a pronounced low velocity zone imply low temperatures throughout most of the upper mantle beneath cratons. With temperatures obtained from forward modelling of seismic velocities (Faul and Jackson, 2005; Jackson and Faul, 2010) cratonic viscosities remain high even at high water contents (Fig. 9). Calculated minimum viscosities in the

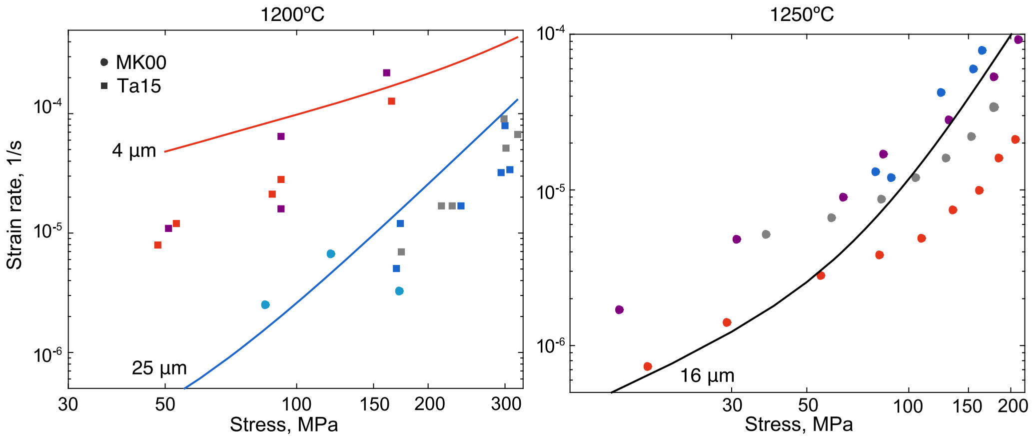

Fig. 8. Deformation data of hydrous San Carlos olivine at two temperatures. Dots represent data from Mei and Kohlstedt (2000b) (300 MPa data only), squares data from Tasaka et al. (2015) (Fo_{90} compositions only). Each colour represents data from one experiment. Lines represent strain rates calculated from Equation (1) with the parameters in Table 2 and a water content of 130 ppm H/Si. The approximate grain sizes relevant for the diffusion creep portions are indicated next to the lines. At 4 µm deformation occurs predominantly in diffusion creep while at 25 µm deformation occurs predominantly in (grain size independent) dislocation creep. Grain sizes for the samples of Mei and Kohlstedt (2000b) range from 15 to 18 µm, the two more coarse-grained samples from Tasaka et al. (2015) have grain sizes of 8 and 25 µm but deform similarly. (For interpretation of the references to colour in this figure legend, the reader is referred to the web version of this article.)

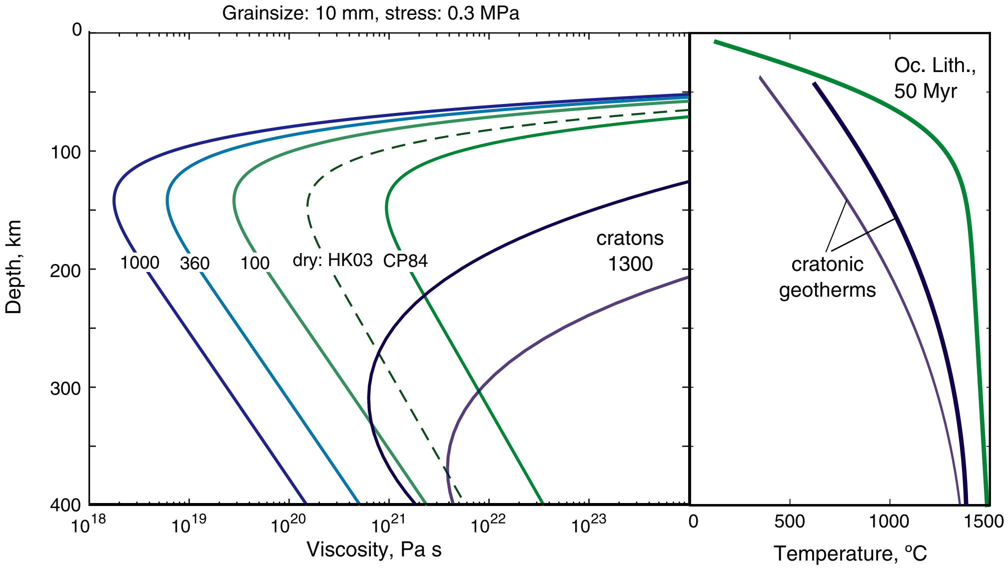

Fig. 9. Viscosity of the Earth's upper mantle as a function of water content calculated with the parameters from Table 2. Temperature for the oceanic case (right panel) corresponds to conductively cooling lithosphere with an age of 50 Myr joined by an adiabat with potential temperature of 1350 °C. For cratons (Yilgarn and Northern Australia) the temperature profiles were constructed by forward modelling observed seismic velocities (Faul and Jackson, 2005; Jackson and Faul, 2010). The numbers show water content (in ppm H/Si). For cratonic temperatures diffusion creep and dislocation creep give very similar strain rates.

upper mantle of order 10^{21} Pa s are consistent with those inferred from geodetic observations for Fennoscandia (Milne et al., 2001) and North America (Tamisea et al., 2007).

7. Conclusions

Experiments with synthetic, Ti-doped and silica-buffered olivine reproduce published parameters for the effect of water on the rheology of olivine. Infrared spectra of the experimental samples show only two absorption bands, at 3572 and 3525 cm^{-1}. These bands appear only in olivine that contains Ti, independent of Si buffering. San Carlos olivine contains Ti, and correspondingly the spectra of untreated samples, and those produced in low water fugacity experiments exhibit these bands. The absence of IR bands related to hydrated M-site vacancies in the products of the present experiments indicates that the Ti-related defects are the cause for the observed dependence of the rheology on water concentration. Hydration of Ti increases the concentration of Si vacancies and therefore the Si diffusivity, consistent with the view that Si diffusion is the rate limiting species for deformation of olivine. Accounting for partitioning between solid phases, undepleted olivine in the upper mantle contains enough Ti to accommodate the expected water content of olivine in the asthenosphere (MORB-source mantle). Viscosities calculated for the upper mantle based on published water contents are consistent with viscosity estimates from the literature, indicating that Ti-related hydrous defects can control the rheology of the upper mantle.

Acknowledgements

This work was in part funded by NSF Grant EAR 1321889 to U.F. and Australian Research Council Grant DP130103848 to I.J, A.B., U.F. and S. Karato. The authors thank Alberto Padrón-Navarta and Joerg Hermann for discussions on infrared spectroscopy, Harri Kokkonen and Hayden Miller for technical assistance, and Frank Brink from the Center of Advanced Microscopy at ANU for help with EBSD.

Reviews by A. Peslier and two anonymous reviewers of an earlier version helped to improve the manuscript.

Appendix A. Infrared spectroscopy

Room-temperature transmission FTIR spectra were recorded both after hotpressing and after deformation for each sample at RSES, ANU using a Bruker Tensor 27 spectrometer fitted with a Bruker Hyperion 2000 microscope, a KBr beam splitter, a Globar light source and a MCT-A detector. The microscope stage and spectrometer were continuously purged by nominally dry air. Spectra were recorded from 600 to 5000 cm^{-1} with a spectral resolution of 4 cm^{-1}. The spectra in this study consist of the average of 128 scans. A 15× objective and a square aperture with a side length of 200 μm were used for all spectra. Spectra were recorded using unpolarised light with approximately 400 μm thick sections that were polished on both sides. The use of thick sections allows averaging of the absorbance over hundreds of crystals (200 μm aperture, mean crystal size ∼25 μm) with an appropriate correction for conversion to water content (Kovacs et al., 2008, see below Equation (A.2)).

Spectra were recorded from the centre of the sample radially outwards to the rim with a spacing of ∼200 μm for a total of 25 to 30 spectra per sample. After the acquisition of each spectrum, an atmospheric compensation correction was applied to remove contributions from traces of water vapour, which improved the signal to noise ratio. Next, the background was fit using a concave rubber band baseline algorithm provided by the software, using three iterations, and subtracted. Alternative methods of background subtraction resulted in water contents that differed only by a few percent (Zhao et al., 2004; Bell et al., 2003). The concave rubber band method is reproducible and has little impact on the absorption bands (Kovacs et al., 2010; Padrón-Navarta et al., 2014).

Concentrations of molecular water and hydroxyl were separately calculated by a Beer–Lambert law. Molecular water was calculated with:

$$C_{H_2O} = \frac{A(\nu = 3450\ \text{cm}^{-1})}{l\,\epsilon}\,\frac{M_{H_2O} \times 10^6}{\rho_{ol}}, \tag{A.1}$$

where C is the concentration in wt. ppm, A is the measured absorbance at 3450 cm^{-1}, l is the sample thickness in cm and ϵ the molar absorption coefficient (115 $\text{L}\,\text{mol}^{-1}\,\text{cm}^{-1}$, Clunie et al., 1966). M_{H_2O} is the molar mass of water (18.02 $\text{g}\,\text{mol}^{-1}$) and ρ_{ol} is the density of olivine (3288 $\text{g}\,\text{l}^{-1}$).

The concentration of bound hydroxyl (in wt. ppm) was calculated from the integrated area under the absorption bands (A_{int}) as:

$$C_{OH} = \frac{A_{int} \times 3k}{l}, \tag{A.2}$$

where k is the site-specific integral molar absorption coefficient, with a value of $k = 0.18$ cm^2 for the Ti-defect site (Kovacs et al., 2010; see also Matveev and Stachel, 2007 and discussion of hydrated defects in Section 5.2). The absence of an absorption band at 3612 cm^{-1} indicates that Si vacancies unrelated to Ti were not protonated (Padrón-Navarta et al., 2014). The orientation factor of 3 relates the total water content to the absorbance from unpolarised spectra of randomly oriented crystals (Kovacs et al., 2008). A_{int} was determined between 3600 and 3450 cm^{-1}:

$$A_{int} = \int_{\nu=3450\ \text{cm}^{-1}}^{\nu=3600\ \text{cm}^{-1}} A(\nu)d\nu - \left\{\frac{[A(\nu = 3600\ \text{cm}^{-1}) + A(\nu = 3450\ \text{cm}^{-1})](3600 - 3450)}{2}\right\}. \tag{A.3}$$

The second term of equation (A.3) subtracts the broad absorption region due to molecular water as indicated in Fig. 4. A_{int} was calculated using the integration tool of the OPUS FTIR control software. As noted by Bell et al. (2003), the integration limits and subtraction of the molecular water are somewhat subjective, but results obtained from different treatments of the spectra typically agree within 5%. The absolute error involving integration limits and background correction is likely larger, with a conservative range from 10–30%.

Volumetric average hydroxyl and molecular water contents ($\overline{C_i}$, where i stands for either molecular or hydroxyl) for each sample were calculated from the respective radial variations after regularising the discrete measurements:

$$\overline{C_i} = \frac{1}{\pi R^2}\int_0^R 2\pi r[H_2O](r)dr, \tag{A.4}$$

where R is the sample radius. The sample averaged molecular water content thus obtained is with one exception significantly smaller than the averaged hydroxyl content. The experiments are water-undersaturated since fH_2O is not buffered. Accordingly we only observe one type of hydrated defect; at saturated conditions and in equilibrium with orthopyroxene, hydrated metal vacancies would also be expected (Berry et al., 2005; Kovacs et al., 2010).

Appendix B. Supplementary material

Supplementary material related to this article can be found online at http://dx.doi.org/10.1016/j.epsl.2016.07.016.

References

Avé Lallemant, H.G., Carter, N.L., 1970. Syntectonic recrystallization of olivine and modes of ow in the upper mantle. Geol. Soc. Am. Bull. 81, 2203–2220.

Bai, Q., Kohlstedt, D.L., 1992. Substantial hydrogen solubility in olivine and implications for water storage in the mantle. Nature 357, 672–674.

Bai, Q., Kohlstedt, D.L., 1993. Effects of chemical environment on the solubility and incorporation mechanism for hydrogen in olivine. Phys. Chem. Miner. 19, 460–471.

Balan, E., Ingrin, J., Delattre, S., Kovacs, I., Blanchard, M., 2011. Theoretical infrared spectrum of OH-defects in forsterite. Eur. J. Mineral. 23, 285–292.

Bell, D.R., Rossman, G.R., Maldener, J., Endisch, D., Rauch, F., 2003. Hydroxide in olivine: a quantitative determination of the absolute amount and calibration of the IR spectrum. J. Geophys. Res. 108. http://dx.doi.org/10.1029/2001JB000679.

Beran, A., Libowitzky, E., 2006. Water in natural mantle minerals II: olivine, garnet and accessory minerals. In: Keppler, H., Smyth, J.R. (Eds.), Water in Nominally Anhydrous Minerals. In: Rev. Mineral. Geochem., vol. 62. Mineralogical Society of America, pp. 169–191.

Berry, A.J., Hermann, J., O'Neill, H.S.C., Foran, G.J., 2005. Fingerprinting the water site in mantle olivine. Geology 33, 869–872. http://dx.doi.org/10.1130/G21759.1.

Berry, A.J., O'Neill, H.S.C., Hermann, J., Scott, D.R., 2007a. The infrared signature of water associated with trivalent cations in olivine. Earth Planet. Sci. Lett. 261, 134–142.

Berry, A.J., Walker, A., Hermann, J., O'Neill, H.S.C., Foran, G., Gale, J., 2007b. Titanium substitution mechanisms in forsterite. Chem. Geol. 242, 176–186.

Bills, B.G., Adams, K.D., Wesnousky, S.G., 2007. Viscosity structure of the crust and upper mantle in western Nevada from isostatic rebound patterns of Lake Lahontan shorelines. J. Geophys. Res. 112, B06405.

Chopra, P.N., Paterson, M.S., 1984. The role of water in the deformation of dunite. J. Geophys. Res. 89, 7861–7876.

Clunie, J.S., Goodman, J., Ogden, C., 1966. Extinction coefficient of water at 2.93μ and water content of black foam films. Nature 209, 1192–1193.

Costa, F., Chakraborty, S., 2008. The effect of water on Si and O diffusion rates in olivine and implications for transport properties and processes in the upper mantle. Phys. Earth Planet. Inter. 166, 11–29.

de Hoog, J.C.M., Gall, L., Cornell, D.H., 2010. Trace-element geochemistry of mantle olivine and application to mantle petrogenesis and geothermobarometry. Chem. Geol. 270, 196–215. http://dx.doi.org/10.1016/j.chemgeo.2009.11.017.

Demouchy, S., Jacobson, S.D., Gaillard, F., Stern, C.R., 2006. Rapid magma ascent recorded by water diffusion profiles in mantle olivine. Geology 34, 429–432. http://dx.doi.org/10.1130/G22386.1.

Dohmen, R., Chakraborty, S., 2007. Fe–Mg diffusion in olivine II: point defect chemistry, change of diffusion mechanisms and a model for calculation of diffusion coefficients in natural olivine. Phys. Chem. Miner. 34, 409–430.

Dohmen, R., Milke, R., 2010. Diffusion in polycrystalline materials: grain boundaries, mathematical models, and experimental data. Rev. Mineral. Geochem. 72, 921–970.

Faul, U.H., Jackson, I., 2005. The seismological signature of temperature and grain size variations in the upper mantle. Earth Planet. Sci. Lett. 234, 119–134.

Faul, U.H., Jackson, I., 2007. Diffusion creep of dry, melt-free olivine. J. Geophys. Res. 110, B04204. http://dx.doi.org/10.1029/2006JB004586.

Fei, H., Hegoda, C., Yamazaki, D., Wiedenbeck, M., Yurimoto, H., Shcheka, S., Katsura, T., 2012. High silicon self-diffusion coefficient in dry forsterite. Earth Planet. Sci. Lett. 345–348, 95–103. http://dx.doi.org/10.1016/j.epsl.2012.06.044.

Fei, H., Wiedenbeck, M., Yamazaki, D., Katsura, T., 2013. Small effect of water on upper-mantle rheology based on silicon self-diffusion coefficients. Nature 498, 213–215. http://dx.doi.org/10.1038/nature12193.

Fleming, K., Martinec, Z., Wolf, D., 2007. Glacial-isostatic adjustment and the viscosity structure underlying the Vatnajökull ice cap, Iceland. Pure Appl. Geophys. 164, 751–768.

Foley, S.F., Prelević, D., Rehfeldt, T., Jacob, D.E., 2013. Minor and trace elements in olivines as probes into early igneous and mantle melting processes. Earth Planet. Sci. Lett. 363, 181–191.

Frey, F.A., Prinz, M., 1978. Ultramafic inclusions from San Carlos, Arizona: petrologic and geochemical data bearing on their petrogenesis. Earth Planet. Sci. Lett. 38, 129–176.

Girard, J., Chen, J., Raterron, P., Holyoke, C.W., 2013. Hydrolytic weakening of olivine at mantle pressure: Evidence of [100](010) slip system softening from single-crystal deformation experiments. Phys. Earth Planet. Inter. 216, 12–20.

Hirth, G., Kohlstedt, D.L., 1995. Experimental constraints on the dynamics of the partially molten upper mantle: 1. Deformation in the diffusion creep regime. J. Geophys. Res. 100, 1981–2001.

Hirth, G., Kohlstedt, D.L., 1996. Water in the oceanic upper mantle: implications for rheology, melt extraction and the evolution of the lithosphere. Earth Planet. Sci. Lett. 144, 93–108.

Hirth, G., Kohlstedt, D.L., 2003. Rheology of the upper mantle and the mantle wedge: a view from the experimentalists. In: Eiler, J. (Ed.), Inside the Subduction Factory. In: Geophys. Monogr., vol. 138. American Geophysical Union, pp. 83–105.

Jackson, I., Faul, U.H., 2010. Grainsize-sensitive viscoelastic relaxation in olivine: towards a robust laboratory-based model for seismological application. Phys. Earth Planet. Inter. 183, 151–163.

Jaoul, O., Poumellec, M., Froidevaux, C., Havette, A., 1981. Silicon diffusion in forsterite: a new constraint for understanding mantle deformation. In: Stacey, F.D., Paterson, M.S., Nicolas, A. (Eds.), Anelasticity in the Earth. In: Geodyn. Ser., vol. 4. American Geophysical Union, pp. 95–100.

Jaques, A.L., Green, D.H., 1980. Anhydrous melting of peridotite at 0–15 kb pressure and the genesis of tholeiitic basalts. Contrib. Mineral. Petrol. 73, 287–310.

Jung, H., Karato, S.I., 2001. Effects of water on the dynamically recrystallized grain size in olivine. J. Struct. Geol. 23, 1337–1344.

Karato, S.I., 1989a. Defects and plastic deformation of olivine. In: Karato, S.I., Toriumi, M. (Eds.), Rheology of Solids and of the Earth. Oxford University Press, pp. 176–208.

Karato, S.I., 1989b. Grain growth kinetics in olivine aggregates. Tectonophysics 168, 255–273.

Karato, S.I., 2008. Deformation of Earth Materials. Cambridge University Press.

Karato, S.I., Jung, H., 2003. Effects of pressure on high-temperature dislocation creep in olivine. Philos. Mag. 83, 401–414.

Karato, S.I., Paterson, M.S., Fitz Gerald, J.D., 1986. Rheology of synthetic olivine aggregates: influence of grain size and water. J. Geophys. Res. 91, 8151–8176.

Keppler, H., Bolfan-Casanova, N., 2006. Thermodynamics of water solubility and partitioning. Rev. Mineral. Geochem. 62, 193–230.

Kohlstedt, D.L., 2006. The role of water in high-temperature rock deformation. Rev. Mineral. Geochem. 62, 377–396.

Kohlstedt, D.L., Mackwell, S.J., 1998. Diffusion of hydrogen and intrinsic point defects in olivine. Z. Phys. Chem. 207, 147–162.

Kohlstedt, D.L., Keppler, H., Rubie, D.C., 1996. Solubility of water in the α, β and γ phases of $(Mg,Fe)_2SiO_4$. Contributions to. Mineral. Petrol. 123, 345–357.

Kovacs, I., Hermann, J., O'Neill, H.S.C., Fitz Gerald, J.D., Sambridge, M., Horvarth, G., 2008. Quantitative absorbance spectroscopy with unpolarized light, part II: Experimental evaluation and development of a protocol for quantitative analysis of mineral IR spectra. Am. Mineral. 93, 765–778.

Kovacs, I., O'Neill, H.S.C., Hermann, J., Hauri, E.H., 2010. Site-specific infrared O–H absorption coefficients for water substitution into olivine. Am. Mineral. 95, 292–299.

Lemaire, C., Kohn, S.C., Brooker, R.A., 2004. The effect of silica activity on the incorporation mechanisms of water in synthetic forsterite: a polarised infrared spectroscopic study. Contrib. Mineral. Petrol. 147, 48–57.

Mackwell, S.J., Kohlstedt, D.L., 1990. Diffusion of hydrogen in olivine: implications for water in the mantle. J. Geophys. Res. 95, 5079–5088.

Mackwell, S.J., Kohlstedt, D.L., Paterson, M.S., 1985. The role of water in the deformation of olivine single crystals. J. Geophys. Res. 90, 11319–11333.

Matveev, S., Stachel, T., 2007. FTIR spectroscopy of OH in olivine: a new tool in kimberlite exploration. Geochim. Cosmochim. Acta 71, 5528–5543.

Matveev, S., O'Neill, H.S.C., Ballhaus, C., Taylor, W.R., Green, D.H., 2001. Effect of silica activity on OH^- IR spectra of olivine: implications for low-$aSiO_2$ mantle metasomatism. J. Petrol. 42, 721–729.

Mei, S., Kohlstedt, D.L., 2000a. Influence of water of plastic deformation of olivine aggregates: 1. Diffusion creep regime. J. Geophys. Res. 105, 21,457–21,469.

Mei, S., Kohlstedt, D.L., 2000b. Influence of water of plastic deformation of olivine aggregates: 2. dislocation creep regime. J. Geophys. Res. 105, 21,471–21,481.

Mei, S., Bai, W., Hiraga, T., Kohlstedt, D.L., 2002. Influence of melt on the creep behavior of olivine-basalt aggregates under hydrous conditions. Earth Planet. Sci. Lett. 201, 491–507.

Michael, P.J., 1988. The concentration, behavior and storage of H_2O in the suboceanic mantle: implications for mantle metasomatism. Geochim. Cosmochim. Acta 52, 555–566.

Miller, G.H., Rossman, G.R., Harlow, G.E., 1987. The natural occurrence of hydroxide in olivine. Phys. Chem. Miner. 14, 461–472.

Milne, G.A., Davis, J.L., Mitrovica, J.X., Scherneck, H.-G., Johansson, J.M., 2001. Space-geodetic constraints on glacial isostatic adjustment in Fennoscandia. Science 291, 2381–2385.

Mosenfelder, J.L., Deligne, N.I., Asimov, P.D., Rossman, G.R., 2006. Hydrogen incorporation in olivine from 2–12 GPa. Am. Mineral. 91, 285–294.

Nakamura, A., Schmalzried, H., 1983. On the nonstoichiometry and point defects of olivine. Phys. Chem. Miner. 10, 27–37.

Padrón-Navarta, J., Hermann, J., O'Neill, H.S.C., 2014. Site-specific hydrogen diffusion rates in forsterite. Earth Planet. Sci. Lett. 392, 100–112.

Peslier, A.H., Woodland, A.B., Bell, D.R., Lazarov, M., 2010. Olivine water contents in the continental lithosphere and the longevity of cratons. Nature 467. http://dx.doi.org/10.1038/nature09317.

Peslier, A.H., Bizimis, M., Matney, M., 2015. Water disequilibrium in olivines from Hawaiian peridotites: recent metasomatism, H diffusion and magma ascent rates. Geochim. Cosmochim. Acta 154, 98–117.

Podolefsky, N.S., Zhong, S., McNamara, A.K., 2004. The anisotropic and rheological structure of the oceanic upper mantle from a simple model of plate shear. Geophys. J. Int. 158, 287–296.

Rubie, D.C., Karato, S., Yan, H., O'Neill, H.S.C., 1993. Low differential stress and controlled chemical environment in multianvil high-pressure experiments. Phys. Chem. Miner. 20, 315–322.

Tamisea, M.E., Mitrovica, J.X., Davis, J.L., 2007. Grace gravity data constrain ancient ice geometries and continental dynamics over Laurentia. Science 316, 881–883.

Tasaka, M., Zimmerman, M.E., Kohlstedt, D.L., 2015. Creep behavior of Fe-bearing olivine under hydrous conditions. J. Geophys. Res. 120, 6039–6057. http://dx.doi.org/10.1002/2015JB012096.

Tenner, T.J., Hirschmann, M.M., Withers, A.C., Ardia, P., 2012. H_2O storage capacity of olivine and low-Ca pyroxene from 10 to 13 GPa: consequences for dehydration melting above the transition zone. Contrib. Mineral. Petrol. 163, 297–316.

Umemoto, K., Wentzcovitch, R., Hirschmann, M.M., Kohlstedt, D.L., Withers, A.C., 2011. A first-principles investigation of hydrous defects and IR frequencies in forsterite: the case for Si vacancies. Am. Mineral. 96, 1475–1479.

Walker, A.M., Hermann, J., Berry, A.J., O'Neill, H.S.C., 2007. Three water sites in upper mantle olivine and the role of titanium in the water weakening mechanism. J. Geophys. Res. 112, B05211. http://dx.doi.org/10.1029/2006JB004620.

Workman, R.R., Hart, S.R., 2005. Major and trace element composition of the depleted MORB mantle (DMM). Earth Planet. Sci. Lett. 231, 53–72. http://dx.doi.org/10.1016/j.epsl.2004.12.005.

Zhao, Y.-H., Ginsberg, S.B., Kohlstedt, D.L., 2004. Solubility of hydrogen in olivine: dependence on temperature and iron content. Contrib. Mineral. Petrol. 147, 155–161.